

Joint Dynamic MRI Reconstruction and Aggregated Motion Estimation with Optical Flow Constraint

Ningning Zhao, Daniel O'Connor, Dan Ruan, Adrian Basarab, Peng Hu, Ke Sheng

Abstract

This paper proposes a novel framework to jointly reconstruct the dynamic magnetic resonance images (DMRI) and estimate the motion vectors from the under-sampled measurements. Due to the inherent motion effects in DMRI acquisition, reconstruction of DMRI using motion estimation/compensation has been studied under a compressed sensing (CS) scheme. In this paper, by embedding the intensity based optical flow (OF) constraint into the traditional CS scheme, we are able to couple the DMRI reconstruction with vector motion estimation. The resulting optimization problem is then solved by a primal-dual algorithm with linesearch due to its efficiency when dealing with non-differentiable problems. Moreover, the proposed framework is capable of handling a wide class of prior information (regularizations) for DMRI reconstruction, such as sparsity, low rank, total variation. In order to reduce the computational cost, the OF constraint is employed in a specific coarse scale. Experiments on various DMRI data, ranging from *in vivo* lung data to simulated phantom, validate the reconstruction quality improvement using the proposed scheme in comparison to several state-of-the-art algorithms.

Index Terms

Ningning Zhao, Daniel O'Connor, Dan Ruan and Ke Sheng are with the department of radiation oncology, University of California, Los Angeles, CA, USA (e-mail: {buaazhaonn, daniel.v.oconnor}@gmail.com, {DRuan, KSheng}@mednet.ucla.edu).

Adrian Basarab is with University of Toulouse, IRIT, CNRS UMR 5505, 118 Route de Narbonne, F-31062, Toulouse Cedex 9, France (e-mail: adrian.basarab@irit.fr).

Hu Peng is with the department of radiology, University of California, Los Angeles, CA, USA (e-mail: PengHu@mednet.ucla.edu).

I. INTRODUCTION

Dynamic magnetic resonance imaging (DMRI) plays an important role in different clinical exams, e.g., cardiovascular, pulmonary, abdominal, perfusion and functional imaging. The reconstruction of DMRI aims at obtaining spatio-temporal MRI sequences in \mathbf{x} - t space, from their measurements acquired in the \mathbf{k} - t space. The acquisition speed of DMRI measurements is limited by the physical constraints, e.g., nuclear relaxation times, gradient strength and slew rate. Thus, the trade-off between spatial and temporal resolution in DMRI reconstruction is challenging. Classical techniques to deal with this issue include echo planar imaging [1], fast low-angle shot imaging [2] and parallel imaging [3].

In recent years, compressed sensing (CS) techniques have demonstrated great success in reducing the acquisition time without degrading image quality, see e.g., [4], [5]. CS theory guarantees an exact recovery of specific signals or images from fewer measurements than the number predicted by the Nyquist limit. This guarantee is based on incoherent measurements that generalize the concept of samples in the standard sampling scheme. Image reconstruction from undersampled (compressed) observations is an ill-posed problem that consequently requires the use of prior information (regularization) to stabilize the solution. The regularizations widely used for DMRI reconstruction include sparsity in transformed domains [6], total variation (TV) penalties [7], low-rank property [8] or a combination of several priors [9]–[11]. Under the CS-based framework, DMRI reconstruction methods can be broadly divided into two categories: offline and online [12]. The online methods reconstruct images for each temporal frame in real time, while the images are reconstructed after all the temporal data have been acquired in the offline methods. Similar to most of CS-based DMRI reconstruction methods, we focus in this paper on the offline approach.

Due to the presence of anatomical motion in DMRI acquisition, combining the motion estimation with the DMRI reconstruction has been already explored in the literature. For example, low rank plus sparse (L+S) matrix decomposition has been successfully applied to DMRI reconstruction in [11], [13]. In these studies, L models the temporally correlated background and S models the dynamic information. In addition, motion estimation/compensation (ME/MC) has been studied in DMRI reconstruction. For instance, [6], [14] proposed to reconstruct DMRI using kt-FOCUSS algorithm with ME/MC. Lingala *et. al.* [15] coupled

the DMRI reconstruction and the inter-frame motion estimation, modelled as an elastic deformation, using a variable splitting algorithm. In [16], extra motion-state dimensions were added for the MRI reconstruction under the CS scheme. In [17], a nonparametric aggregated motion estimation (AME) was incorporated for real-time DMRI reconstruction.

In this paper, we propose a general framework to jointly estimate the DMRI and the aggregated motion vectors by embedding an intensity-based optical flow (OF) constraint into the CS framework. In order to reduce the computational cost, the OF constraint is exploited at a coarse scale. Moreover, an affine model is employed to model local tissue deformations [18]. The resulting formulated problem is addressed using the primal-dual algorithm with linesearch [19], known to efficiently handle non-differentiable convex optimization problems. Experimental phantom and *in vivo* DMRI reconstruction results demonstrate the superiority of the proposed framework over several state-of-the-art algorithms.

The remainder of this paper is organized as follows. In Section II, we describe the background related with the proposed framework. The variational problem is formulated in Section III. Section IV details the proposed algorithm and relevant derivations. Section V gives the experimental results. Conclusions and perspectives are reported in Section VI.

II. BACKGROUND

A. DMRI measurements

The DMRI measurements acquired in the \mathbf{k} - t space are denoted as $\mathbf{b}(\mathbf{k}, t)$, which can be modelled by

$$b(\mathbf{k}, t) = \int_{\mathbf{x}} f(\mathbf{x}, t) \exp(-j\mathbf{k}^T \mathbf{x}) d\mathbf{x} + n(\mathbf{k}, t) \quad (1)$$

where $f(\mathbf{x}, t)$ is the spatio-temporal MRI sequence, $n(\mathbf{k}, t)$ represents the measurement noise, $\mathbf{x} = [x, y]$ and t are the spatial and temporal coordinates and \mathbf{k} is the 2D frequency variable. Note that although the image formation model is valid for any number of spatial dimensions, to simplify the description, we only consider the $2D + t$ case in this paper [20]. The above expression can be rewritten in a matrix form as below

$$\mathbf{b} = \mathcal{A}(\mathbf{f}) + \mathbf{n} \quad (2)$$

where the measurement operator \mathcal{A} represents the partial/masked Fourier transform on specific sampling locations, the DMRI sequence \mathbf{f} is of size $m \times n \times T$, where m, n are the spatial dimensions of each frame and T is the total frame number.

B. Optical flow

Denoting $\mathbf{f}(\mathbf{x}, t_0)$ as a reference frame acquired at time t_0 , the brightness/intensity constancy constraint in DMRI is formulated as

$$\mathbf{f}(\mathbf{x}, t) = \mathbf{f}(\mathbf{x} - \mathbf{d}(\mathbf{x}, t), t_0) \quad (3)$$

where $\mathbf{d}(\mathbf{x}, t) = [\mathbf{u}(\mathbf{x}, t), \mathbf{v}(\mathbf{x}, t)]^T$ is the displacement field between the reference image and the t th temporal frame $\mathbf{f}(\mathbf{x}, t)$, $\mathbf{u}(\mathbf{x}, t)$ and $\mathbf{v}(\mathbf{x}, t)$ are the horizontal and vertical components of the displacement field. Under the hypothesis of small displacements, the first-order Taylor approximation can be used to replace the nonlinear intensity profile, *i.e.*,

$$\mathbf{f}(\mathbf{x} - \mathbf{d}(\mathbf{x}, t), t_0) \approx \mathbf{f}_0 - \partial_x \mathbf{f}_0 \mathbf{u}(\mathbf{x}, t) - \partial_y \mathbf{f}_0 \mathbf{v}(\mathbf{x}, t) \quad (4)$$

where the reference frame $\mathbf{f}_0 \triangleq \mathbf{f}(\mathbf{x}, t_0)$, $\partial_x \mathbf{f}_0$ and $\partial_y \mathbf{f}_0$ are the partial derivatives of the reference frame with respect to x and y . Combining (3) and (4), the traditional optical flow (OF) constraint equation is given by

$$\mathbf{f}(\mathbf{x}, t) - \mathbf{f}_0 + \partial_x \mathbf{f}_0 \mathbf{u}(\mathbf{x}, t) + \partial_y \mathbf{f}_0 \mathbf{v}(\mathbf{x}, t) = 0. \quad (5)$$

To estimate the motion vectors $\mathbf{d}(\mathbf{x}, t) = [\mathbf{u}(\mathbf{x}, t), \mathbf{v}(\mathbf{x}, t)]^T$, a dedicated cost function can be formulated globally (on the entire image) or locally (by patches) using region-based matching [18], [21].

a) OF with brightness variation: Since image intensities are very unlikely to be constant over time as suggested in (3), an illumination variable $\mathbf{q}(\mathbf{x}, t)$ has been introduced to model the spatio-temporal brightness variation, see e.g., [22], [23]. The OF equation can thus be rewritten as

$$\mathbf{f}(\mathbf{x}, t) - \mathbf{f}_0 + \partial_x \mathbf{f}_0 \mathbf{u}(\mathbf{x}, t) + \partial_y \mathbf{f}_0 \mathbf{v}(\mathbf{x}, t) + \mu \mathbf{q}(\mathbf{x}, t) = 0 \quad (6)$$

where μ controls the influence of the illumination term \mathbf{q} .

b) Affine model: It is important to note that the motion patterns in medical images can be very complex due to tissue deformations such as rotation, expansion, contraction and shear. In order to accurately describe these motion patterns, the affine model has been extensively used in the related literature, see e.g., [18], [24], [25]. Based on the affine model, the motion vectors at position (x, y) for the t th frame are expressed by

$$\mathbf{u}(x, y, t) = \mathbf{u}_0(x, y, t) + \mathbf{u}_1(x, y, t)x + \mathbf{u}_2(x, y, t)y \quad (7)$$

$$\mathbf{v}(x, y, t) = \mathbf{v}_0(x, y, t) + \mathbf{v}_1(x, y, t)x + \mathbf{v}_2(x, y, t)y \quad (8)$$

where $\mathbf{u}_0, \mathbf{u}_1, \mathbf{u}_2$ and $\mathbf{v}_0, \mathbf{v}_1, \mathbf{v}_2$ are the affine parameters defining the motion of pixel at position (x, y) in frame t w.r.t. the reference frame \mathbf{f}_0 [18].

c) *Weighted OF*: The weighted OF equation, widely explored for motion estimation, see e.g., [18], [24]–[26], can be expressed as below

$$\int_{\mathbf{x}} \mathbf{w}(\mathbf{x} - \mathbf{x}_0) [\mathbf{f}(\mathbf{x}, t) - \mathbf{f}_0 + \partial_x \mathbf{f}_0 \mathbf{u}(\mathbf{x}, t) + \partial_y \mathbf{f}_0 \mathbf{v}(\mathbf{x}, t)] d\mathbf{x} \quad (9)$$

where \mathbf{w} is a window function centered at \mathbf{x}_0 . Given the window weighted OF equation, the motion vectors are estimated locally by assuming they are constant within a spatial neighbourhood. B-spline-based windows, *i.e.*, $\mathbf{w}(\mathbf{x}) = \beta^n(x)\beta^n(y)$, where $\beta^n(\cdot)$ is a symmetrical B-spline function of degree $n \in \mathbb{N}$, have been shown to be adapted to medical images [18], [25]. Varying the B-spline degree changes the size of \mathbf{w} . Moreover, the displacement field can be estimated at different scales by dilating and shifting the window function \mathbf{w} . Specifically, at a coarse spatial scale j , the window function is given by

$$\mathbf{w}^{(j)}(\mathbf{x} - \mathbf{x}_0) = \mathbf{w}\left(\frac{\mathbf{x} - 2^j \mathbf{x}_0}{2^j}\right) \quad (10)$$

Since the window function at scale j is dilated by a factor 2^j , the calculation of (9) at scale j corresponds to subsampling the inner product at the finest scale by a factor 2^j .

C. Proximal operator

The proximal operator of a lower semicontinuous (l.s.c.) function g is defined as

$$\text{prox}_{sg}(p) = \arg \min_x g(x) + \frac{1}{2s} \|x - p\|^2 \quad (11)$$

Note that the proximal operator calculation (11) always has a unique solution. One important property of the proximal operator is the Moreau's decomposition formula given by

$$\text{prox}_{sg^*}(p) = p - s \text{prox}_{s^{-1}g}\left(\frac{p}{s}\right). \quad (12)$$

where g^* is the convex conjugate of function g . Moreau's decomposition builds the relationship between the proximal operator of a l.s.c. function g and the proximal operator of its conjugate [27], [28].

D. Primal-dual algorithm

Primal-dual algorithms (PDAs) have been widely explored for non-smooth convex optimization problems, see e.g., [23], [28]–[30]. Given an optimization problem as below

$$\min_{\mathbf{y}} g(\mathbf{C}\mathbf{y}) + h(\mathbf{y}) \quad (13)$$

where \mathbf{C} is a continuous linear operator, h and g are proper, convex and l.s.c. functions, the corresponding primal-dual/saddle-point problem is expressed by

$$\min_{\mathbf{y}} \max_{\mathbf{z}} \langle \mathbf{C}\mathbf{y}, \mathbf{z} \rangle + h(\mathbf{y}) - g^*(\mathbf{z}) \quad (14)$$

where $\langle \cdot, \cdot \rangle$ is the inner product, g^* is the conjugate of function g and \mathbf{z} is the dual variable. PDA seeks a solution $(\hat{\mathbf{y}}, \hat{\mathbf{z}})$ of the problem (14) by alternating proximal gradient steps with respect to the primal and dual variables. Algorithm 1 summarizes the standard PDA. Note that the stepsize parameters in PDA need to satisfy the relationship $s\sigma\|\mathbf{C}\| \leq 1$ to ensure the convergence. Different variants of Algorithm 1 have been proposed more recently to tune the stepsize parameters adaptively and/or speed up the existing algorithms, see e.g., [19], [29]. Algorithm 2 summarizes the PDA with linesearch (PDAL), which accelerates the traditional PDA.

Algorithm 1 Primal Dual Algorithm (PDA)

Require: $\mathbf{y}^0, \mathbf{z}^0, \sigma, s$

- 1: **for** $k = 1 \dots$ **do**
 - 2: $\mathbf{y}^k = \text{prox}_{\sigma h}(\mathbf{y}^{k-1} - \sigma \mathbf{C}^T \mathbf{z}^{k-1})$
 - 3: $\mathbf{z}^k = \text{prox}_{s g^*}(\mathbf{z}^{k-1} + s \mathbf{C}(2\mathbf{y}^k - \mathbf{y}^{k-1}))$
 - 4: **until** stopping criterion is satisfied.
-

III. PROBLEM FORMULATION

In order to reconstruct the DMRI and estimate the displacement field simultaneously, we first replicate the reference frame T times and stack them into a cube. The resulting cube, having the same size as \mathbf{f} , is denoted as $\bar{\mathbf{f}}_0$. The problem can then be formulated in a variational framework as below

$$\begin{aligned} \min_{\mathbf{f}, \mathbf{d}, \mathbf{q}} & \|\mathcal{A}(\mathbf{f}) - \mathbf{b}\|_2^2 + \eta \phi(\mathcal{T}\mathbf{f}) + \tau \|\mathcal{O}\mathcal{F}_{\mathbf{w}(\gamma)}(\mathbf{f}, \bar{\mathbf{f}}_0, \mathbf{d}, \mathbf{q})\|_1 \\ & + \psi(\mathbf{d}) + \lambda \|\nabla \mathbf{q}\|_1 \end{aligned} \quad (15)$$

where $\phi(\mathcal{T}\mathbf{f})$ is the regularization term incorporating prior information about the DMRI, \mathcal{T} is a given transform, $\psi(\mathbf{d})$ is a regularization function aiming at smoothing the displacement fields and η, τ, γ and λ are hyperparameters weighting the importance of each term.

Algorithm 2 Primal Dual Algorithm with linesearch (PDAL)

Require: $\mathbf{y}^0, \mathbf{z}^0, \sigma^0, s, \alpha > 0, \epsilon \in (0, 1), \rho \in (0, 1)$

- 1: Set $\theta^0 = 1$.
 - 2: **for** $k = 1 \dots$ **do**
 - 3: $\mathbf{y}^k = \text{prox}_{\sigma^{k-1}h}(\mathbf{y}^{k-1} - \sigma^{k-1}\mathbf{C}^T\mathbf{z}^{k-1})$
 - 4: Choose any $\sigma^k \in [\sigma^{k-1}, \sigma^{k-1}\sqrt{1 + \theta^{k-1}}]$
 - 5: ***Linesearch***
 - 6: $\theta^k = \frac{\sigma^k}{\sigma^{k-1}}$
 - 7: $\bar{\mathbf{y}}^k = \mathbf{y}^k + \theta^k(\mathbf{y}^k - \mathbf{y}^{k-1})$
 - 8: $\mathbf{z}^k = \text{prox}_{\alpha\sigma^k g^*}(\mathbf{z}^{k-1} + \alpha\sigma^k\mathbf{C}\bar{\mathbf{y}}^k)$
 - 9: **if** $\sqrt{\alpha}\sigma^k\|\mathbf{C}^T\mathbf{z}^k - \mathbf{C}^T\mathbf{z}^{k-1}\| \leq \epsilon\|\mathbf{z}^k - \mathbf{z}^{k-1}\|$ **then**
 - 10: Break linesearch
 - 11: **else**
 - 12: $\sigma^k = \sigma^k\rho$ and go to ***linesearch*** (step 5)
 - 13: Until stopping criterion is satisfied.
-

$\mathcal{OF}_{\mathbf{w}^{(j)}}(\mathbf{f}, \bar{\mathbf{f}}_0, \mathbf{d}, \mathbf{q})$ is the weighted OF constraint at scale j , whose expression is

$$\begin{aligned}
 & \mathcal{OF}_{\mathbf{w}^{(j)}}(\mathbf{f}, \bar{\mathbf{f}}_0, \mathbf{d}, \mathbf{q}) \\
 &= \langle \mathbf{f} - \bar{\mathbf{f}}_0 \rangle_{\mathbf{w}^{(j)}} + \langle \partial_x \bar{\mathbf{f}}_0 \rangle_{\mathbf{w}^{(j)}} \mathbf{u} + \langle \partial_y \bar{\mathbf{f}}_0 \rangle_{\mathbf{w}^{(j)}} \mathbf{v} + \mu \mathbf{q} \\
 &= \langle \mathbf{f} - \bar{\mathbf{f}}_0 \rangle_{\mathbf{w}^{(j)}} + \langle \partial_x \bar{\mathbf{f}}_0 \rangle_{\mathbf{w}^{(j)}} \mathbf{u}_0 + \langle x \partial_x \bar{\mathbf{f}}_0 \rangle_{\mathbf{w}^{(j)}} \mathbf{u}_1 \\
 &\quad + \langle y \partial_x \bar{\mathbf{f}}_0 \rangle_{\mathbf{w}^{(j)}} \mathbf{u}_2 + \langle \partial_y \bar{\mathbf{f}}_0 \rangle_{\mathbf{w}^{(j)}} \mathbf{v}_0 + \langle x \partial_y \bar{\mathbf{f}}_0 \rangle_{\mathbf{w}^{(j)}} \mathbf{v}_1 \\
 &\quad + \langle y \partial_y \bar{\mathbf{f}}_0 \rangle_{\mathbf{w}^{(j)}} \mathbf{v}_2 + \mu \mathbf{q}
 \end{aligned} \tag{16}$$

where $\langle \mathbf{r} \rangle_{\mathbf{w}^{(j)}}$ is the weighted average of variable $\mathbf{r} \in \{\mathbf{f} - \bar{\mathbf{f}}_0, \partial_x \bar{\mathbf{f}}_0, x \partial_x \bar{\mathbf{f}}_0, y \partial_x \bar{\mathbf{f}}_0, \partial_y \bar{\mathbf{f}}_0, x \partial_y \bar{\mathbf{f}}_0, y \partial_y \bar{\mathbf{f}}_0\}$ at scale j , which is given by

$$\langle \mathbf{r} \rangle_{\mathbf{w}^{(j)}} = \int_{\mathbf{x}} \mathbf{w}^{(j)}(\mathbf{x} - \mathbf{x}_0) \mathbf{r}(\mathbf{x}) d\mathbf{x}. \tag{17}$$

In this paper, the window function is constructed with B-spline functions as shown in Section II-B. The calculation of (17) is related to the multi-resolution theory. Further details can be found in [18], [31].

In order to smooth the displacement fields, total variation regularization is used for the

motion vectors and the illumination variable. Considering anisotropic TV, we have

$$\psi(\mathbf{d}) = \gamma \sum_{i=0}^2 \|\nabla \mathbf{u}_i\|_1 + \gamma \sum_{i=0}^2 \|\nabla \mathbf{v}_i\|_1 \quad (18)$$

where

$$\|\nabla \cdot\|_1 = \sum_{i,j} |(\nabla_x \cdot)_{i,j}| + |(\nabla_y \cdot)_{i,j}| \quad (19)$$

with

$$(\nabla_x \cdot)_{i,j} = \begin{cases} (\cdot)_{i+1,j} - (\cdot)_{i,j} & \text{if } i < m \\ 0 & \text{if } i = m \end{cases} \quad (20)$$

$$(\nabla_y \cdot)_{i,j} = \begin{cases} (\cdot)_{i,j+1} - (\cdot)_{i,j} & \text{if } j < n \\ 0 & \text{if } j = n \end{cases} \quad (21)$$

IV. PROPOSED ALGORITHM

Since the problem formulated in (15) is non-differentiable, the PDA is explored to solve it. We first rewrite (15) as a sum of ten l.s.c. functions as below

$$\min_{\mathbf{y}} g(\mathbf{C}\mathbf{y}) = \sum_{l=1}^{10} g_l(\mathbf{C}_l \mathbf{y}) \triangleq \sum_{l=1}^{10} g_l(\boldsymbol{\Omega}_l) \quad (22)$$

where $\boldsymbol{\Omega}_l = \mathbf{C}_l \mathbf{y}$, $\mathbf{y} = [\mathbf{f}, \mathbf{u}_0, \mathbf{u}_1, \mathbf{u}_2, \mathbf{v}_0, \mathbf{v}_1, \mathbf{v}_2, \mathbf{q}]^T$ is the variable to be estimated, the matrix \mathbf{C} is expressed in (23) and the ten functions are expressed in (24).

$$\mathbf{C} = [\mathbf{C}_1, \mathbf{C}_2, \mathbf{C}_3, \mathbf{C}_4, \mathbf{C}_5, \mathbf{C}_6, \mathbf{C}_7, \mathbf{C}_8, \mathbf{C}_9, \mathbf{C}_{10}]$$

$$= \begin{bmatrix} \mathcal{A} & 0 & 0 & 0 & 0 & 0 & 0 & 0 \\ \langle \cdot \rangle_{\mathbf{w}^{(j)}} & \langle \partial_x \bar{\mathbf{f}}_0 \rangle_{\mathbf{w}^{(j)}} & \langle x \partial_x \bar{\mathbf{f}}_0 \rangle_{\mathbf{w}^{(j)}} & \langle y \partial_x \bar{\mathbf{f}}_0 \rangle_{\mathbf{w}^{(j)}} & \langle \partial_y \bar{\mathbf{f}}_0 \rangle_{\mathbf{w}^{(j)}} & \langle x \partial_y \bar{\mathbf{f}}_0 \rangle_{\mathbf{w}^{(j)}} & \langle y \partial_y \bar{\mathbf{f}}_0 \rangle_{\mathbf{w}^{(j)}} & \mu \mathbf{I} \\ \mathcal{T} & 0 & 0 & 0 & 0 & 0 & 0 & 0 \\ 0 & \nabla & 0 & 0 & 0 & 0 & 0 & 0 \\ 0 & 0 & \nabla & 0 & 0 & 0 & 0 & 0 \\ 0 & 0 & 0 & \nabla & 0 & 0 & 0 & 0 \\ 0 & 0 & 0 & 0 & \nabla & 0 & 0 & 0 \\ 0 & 0 & 0 & 0 & 0 & \nabla & 0 & 0 \\ 0 & 0 & 0 & 0 & 0 & 0 & \nabla & 0 \\ 0 & 0 & 0 & 0 & 0 & 0 & 0 & \nabla \end{bmatrix} \quad (23)$$

$$\begin{cases} g_1(\mathbf{\Omega}_1) = \frac{1}{2} \|\mathbf{\Omega}_1 - \mathbf{b}\|_2^2, \\ g_2(\mathbf{\Omega}_2) = \tau \|\mathbf{\Omega}_2 - \langle \bar{\mathbf{f}}_0 \rangle_{\mathbf{w}^{(j)}}\|_1, \\ g_3(\mathbf{\Omega}_3) = \eta \phi(\mathbf{\Omega}_3), \\ g_l(\mathbf{\Omega}_d) = \gamma \|\mathbf{\Omega}_d\|_1, \text{ for } d = 4, \dots, 9, \\ g_{10}(\mathbf{\Omega}_{10}) = \lambda \|\mathbf{\Omega}_{10}\|_1. \end{cases} \quad (24)$$

By introducing the dual variables $\mathbf{z} = [\mathbf{z}_1, \dots, \mathbf{z}_{10}]^T$, the PDA iteration for problem (22) can be summarized as follows

$$\begin{aligned} & \text{For } k = 0, \dots \\ & \begin{cases} \mathbf{y}^k = \mathbf{y}^{k-1} - \sigma \left(\sum_{l=1}^{10} \mathbf{C}_l^T \mathbf{z}_l^{k-1} \right) \\ \mathbf{z}_l^k = \text{prox}_{sg_l^*}(\tilde{\mathbf{z}}_l^{k-1}) \\ \quad = \text{prox}_{sg_l^*}(\mathbf{z}_l^{k-1} + s \mathbf{C}_l (2\mathbf{y}^k - \mathbf{y}^{k-1})) \end{cases} \end{aligned} \quad (25)$$

where the adjoints of the matrices \mathbf{C}_l ($l \in 1, \dots, 10$) are expressed as below

$$\begin{cases} \mathbf{C}_1^T = [\mathcal{A}^T, 0, 0, 0, 0, 0, 0, 0]^T, \\ \mathbf{C}_2^T = [\langle \cdot \rangle_{\mathbf{w}^{(j)T}}, \langle \partial_x \bar{\mathbf{f}}_0 \rangle_{\mathbf{w}^{(j)}}, \langle x \partial_x \bar{\mathbf{f}}_0 \rangle_{\mathbf{w}^{(j)}}, \langle y \partial_x \bar{\mathbf{f}}_0 \rangle_{\mathbf{w}^{(j)}}, \\ \quad \langle \partial_y \bar{\mathbf{f}}_0 \rangle_{\mathbf{w}^{(j)}}, \langle x \partial_y \bar{\mathbf{f}}_0 \rangle_{\mathbf{w}^{(j)}}, \langle y \partial_y \bar{\mathbf{f}}_0 \rangle_{\mathbf{w}^{(j)}}, \mu \mathbf{1}]^T, \\ \mathbf{C}_3^T = [\mathcal{T}^T, 0, 0, 0, 0, 0, 0, 0]^T, \\ \mathbf{C}_4^T = [0, \nabla^T, 0, 0, 0, 0, 0, 0]^T, \\ \mathbf{C}_5^T = [0, 0, \nabla^T, 0, 0, 0, 0, 0]^T, \\ \mathbf{C}_6^T = [0, 0, 0, \nabla^T, 0, 0, 0, 0]^T, \\ \mathbf{C}_7^T = [0, 0, 0, 0, \nabla^T, 0, 0, 0]^T, \\ \mathbf{C}_8^T = [0, 0, 0, 0, 0, \nabla^T, 0, 0]^T, \\ \mathbf{C}_9^T = [0, 0, 0, 0, 0, 0, \nabla^T, 0]^T, \\ \mathbf{C}_{10}^T = [0, 0, 0, 0, 0, 0, 0, \nabla^T]^T. \end{cases} \quad (26)$$

The calculation of the proximal operator of g_l^* is given by

$$\begin{cases} \text{prox}_{sg_1^*}(\tilde{\mathbf{z}}_1) = \frac{\tilde{\mathbf{z}}_1 - s\mathbf{b}}{1+s}, \\ \text{prox}_{sg_2^*}(\tilde{\mathbf{z}}_2) = \text{Proj}_{\tau P}(\tilde{\mathbf{z}}_2 - s \langle \bar{\mathbf{f}}_0 \rangle_{\mathbf{w}^{(j)}}), \\ \text{prox}_{sg_d^*}(\tilde{\mathbf{z}}_d) = \text{Proj}_{\gamma P}(\tilde{\mathbf{z}}_d), \text{ for } d = 4, \dots, 9, \\ \text{prox}_{sg_{10}^*}(\tilde{\mathbf{z}}_{10}) = \text{Proj}_{\lambda P}(\tilde{\mathbf{z}}_{10}). \end{cases} \quad (27)$$

where $\text{Proj}_{\tau P}$ is a projector onto the convex set (Euclidean ℓ^2 -ball) $\tau P = \{\|p\|_\infty \leq \tau\}$, where $\|p\|_\infty = \max_{i,j} |p_{i,j}|$. In practice, this projector can be computed using the straightforward formula

$$\text{Proj}_{\tau P}(p) = \frac{p}{\max\{\tau, |p|\}}. \quad (28)$$

A. Prior of DMRI \mathbf{f}

The computation of $\text{prox}_{sg_3^*}(\tilde{\mathbf{z}}_3)$ depends on the expression of the prior for DMRI, i.e., $\phi(\mathbf{f})$. In this paper, several widely used priors for DMRI images are investigated.

1) *Sparsity prior in the temporal frequency domain:* Since different frames are temporally correlated in DMRI, it is reasonable to assume that these frames are sparse in the transform domain, e.g., the temporal Fourier transform domain [13], [15]. Specifically, the prior of \mathbf{f} is given by

$$g_3(\Omega_3) = \eta\phi(\mathbf{C}_3\mathbf{y}) = \eta\|\mathcal{F}\mathbf{f}\|_1 \quad (29)$$

where \mathcal{F} represents the temporal Fourier transform. The proximal operator of the conjugate function $g_3^*(\cdot)$ is a projector on the Euclidean ℓ^2 -ball given by

$$\text{prox}_{sg_3^*}(\tilde{\mathbf{z}}_3) = \text{Proj}_{\eta P}(\tilde{\mathbf{z}}_3) = \frac{\tilde{\mathbf{z}}_3}{\max\{\eta, |\tilde{\mathbf{z}}_3|\}} \quad (30)$$

2) *TV prior:* In order to constrain the DMRI to be piecewise smooth, TV prior is considered, see e.g., [7], [9]. The TV prior of \mathbf{f} is given by

$$g_3(\Omega_3) = \eta\phi(\mathbf{C}_3\mathbf{y}) = \eta\|\nabla\mathbf{f}\|_1 \quad (31)$$

The spatial TV prior for \mathbf{f} is expressed in (32). The TV prior in both spatial and temporal domain is given by (33).

$$\|\nabla\mathbf{f}\|_1 = \sum_{i,j} |(\nabla_x\mathbf{f})_{i,j}| + |(\nabla_y\mathbf{f})_{i,j}|. \quad (32)$$

$$\|\nabla\mathbf{f}\|_1 = \sum_{i,j,t} |(\nabla_x\mathbf{f})_{i,j,t}| + |(\nabla_y\mathbf{f})_{i,j,t}| + |(\nabla_t\mathbf{f})_{i,j,t}|. \quad (33)$$

The proximal operator of the conjugate function $g_3^*(\cdot)$ is also a projector on the Euclidean ℓ^2 -ball [32].

3) *Low rank prior*: Low rank penalty has been widely exploited in MRI reconstruction [9], [13], [33]. Note that the low rank penalty is a non-convex function. Thus, it is often replaced by the nuclear norm, which is a convex relaxation of the low rank penalty. The nuclear norm prior for \mathbf{f} is given by

$$g_3(\mathbf{\Omega}_3) = \eta\phi\|\mathbf{C}_3\mathbf{y}\|_1 = \eta\|\mathbf{f}\|_* \quad (34)$$

Although $\text{prox}_{s g_3^*}(\cdot)$ is not attainable directly, we can compute it using the proximal operator of the nuclear norm and the Moreau decomposition formula (12). The proximal operator of the nuclear norm can be calculated using the singular value thresholding (SVT) formula

$$\text{prox}_{s^{-1}g_3}(M) = \text{prox}_{\frac{\eta}{s}\|\cdot\|_*}(M) = U\tilde{\Sigma}V^H, \quad (35)$$

where $M = U\Sigma V^H$ is the singular value decomposition of M and $\tilde{\Sigma}$ is a diagonal matrix whose j th diagonal entry can be computed by applying the soft thresholding/shrinkage operator to the j th singular value of M . Explicitly,

$$\tilde{\Sigma}_j = \text{sgn}(\Sigma_j) \max(|\Sigma_j| - \frac{\eta}{s}, 0) \quad (36)$$

where $\text{sgn}(\cdot)$ is the classical sign function.

4) *Joint priors*: More recently, joint priors have been considered for DMRI reconstruction. For example, the low rank plus spatial and temporal TV priors (37) were considered in [9]. In [13], the low rank plus temporal sparsity priors (38) were explored.

$$g_3(\mathbf{\Omega}_3) = \eta\|\mathbf{f}\|_* + \nu\|\nabla\mathbf{f}\|_1 \quad (37)$$

$$g_3(\mathbf{\Omega}_3) = \eta\|\mathbf{f}\|_* + \nu\|\mathcal{W}\mathbf{f}\|_1 \quad (38)$$

Note that $\mathcal{T} = [\mathbf{I}, \nabla]^T$ for (37), while $\mathcal{T} = [\mathbf{I}, \mathcal{W}]^T$ for (38), where \mathbf{I} is an identity matrix and \mathcal{W} represents a specific transform, e.g., the temporal Fourier transform. The proximal operator of g_3 is then given by

$$\text{prox}_{s^{-1}g_3}(\tilde{\mathbf{z}}_3) = \begin{bmatrix} \text{prox}_{s^{-1}\eta\|\cdot\|_*}(\tilde{\mathbf{z}}_3) \\ \text{prox}_{s^{-1}\nu\|\cdot\|_1}(\tilde{\mathbf{z}}_3) \end{bmatrix}. \quad (39)$$

B. Proposed algorithm

The proposed PDAL algorithm to jointly reconstruct the DMRI and estimate the motion vectors (denoted as J-PDAL) is summarized in Algorithm 3. Note that the reference frame \mathbf{f}_0 can be obtained from fully sampled data. Furthermore, the concept of the reference frame

has been already used in the DMRI reconstruction, see e.g., [14]. The stopping criterion used in this paper is given by

$$\frac{|L(\mathbf{y}^{k+1}) - L(\mathbf{y}^k)|}{L(\mathbf{y}^k)} < 10^{-4} \quad (40)$$

where $L(\mathbf{y})$ is the cost function. The stopping tolerance is 10^{-4} in this paper.

Algorithm 3 Joint MRI reconstruction and motion estimation using PDAL (J-PDAL)

Require: $\mathbf{y}^0 = [\mathbf{f}^0, \mathbf{u}_0^0, \mathbf{u}_1^0, \mathbf{u}_2^0, \mathbf{v}_0^0, \mathbf{v}_1^0, \mathbf{v}_2^0, \mathbf{q}^0]$, \mathbf{z}_l^0 , $l \in \{1 \dots 10\}$, $\sigma^0 > 0$, $\alpha > 0$, $\epsilon \in (0, 1)$,

$\rho \in (0, 1)$

1: Set $\theta^0 = 1$

2: **for** $k = 1 \dots$ **do** ▷ Update $\mathbf{y} = [\mathbf{f}, \mathbf{u}_0, \mathbf{u}_1, \mathbf{u}_2, \mathbf{v}_0, \mathbf{v}_1, \mathbf{v}_2, \mathbf{q}]$

3: $\mathbf{y}^k = \mathbf{y}^{k-1} - \sigma^{k-1} (\sum_{l=1}^{10} \mathbf{C}_l^T \mathbf{z}_l^{k-1})$

4: Choose any $\sigma^k \in [\sigma^{k-1}, \sigma^{k-1} \sqrt{1 + \theta^{k-1}}]$

5: ***Linesearch*** ▷ Start linesearch

6: $\bar{\mathbf{y}}^k = \mathbf{y}^k + \theta^k (\mathbf{y}^k - \mathbf{y}^{k-1})$

7: **for** $l=1, \dots, 10$ **do**

8: $\mathbf{z}_l^k = \text{prox}_{\alpha\sigma^k g_l^*}(\mathbf{z}_l^{k-1} + s\mathbf{C}_l \bar{\mathbf{y}}^k)$ ▷ Update \mathbf{z}_l by calculating the proximal operator of $g_l^*(\cdot)$

9: **if** $\sqrt{\alpha}\sigma^k \|\mathbf{C}^T \mathbf{z}^k - \mathbf{C}^T \mathbf{z}^{k-1}\| \leq \epsilon \|\mathbf{z}^k - \mathbf{z}^{k-1}\|$ **then**

10: break the linesearch ▷ Break linesearch

11: **else**

12: $\sigma^k = \sigma^k \rho$ and go to ***linesearch***

13: Until stopping criterion is satisfied. ▷ Stopping criterion

V. EXPERIMENTAL RESULTS

Experiments were conducted on various datasets to assess the performance of the proposed algorithm. The datasets employed in this section include: i) PINCAT numerical phantom¹ [9], [34]; ii) *in vivo* coronal and sagittal lung MRI. A performance comparison between the proposed joint framework J-PDAL and the traditional DMRI reconstruction framework without motion estimation (solved using fast iterative shrinkage-thresholding algorithm (FISTA)

¹The PINCAT data can be downloaded from http://user.engineering.uiowa.edu/~jcb/software/ktslr_matlab/Software.html. More details about the parameters used for PINCAT can be found in [9].

with linesearch [19] due to its computational efficiency) was carried out. Different image regularizations were used for both schemes, including i) sparsity in the temporal frequency domain (denoted as “ ℓ_1 ”), ii) TV prior (denoted as “TV”), iii) low rank in the spatial domain (denoted as “low rank”), iv) combination of low rank and sparsity in temporal frequency domain (denoted as “l+s”), v) combination of low rank and TV prior (denoted as “l+TV”). Moreover, the proposed J-PDAL was also compared with different state-of-the-art algorithms in terms of the DMRI reconstruction quality, including kt-SLR [9], L+S [13] and DC-CS [15].

Note that the regularization parameters in all the algorithms were tuned to their optical values by cross validation. The initial guess of all the algorithms implemented in this paper was chosen by

$$\mathbf{f}^0 = \mathcal{A}^T(\mathbf{b}) \quad (41)$$

where \mathbf{b} is the observation in k - t space. The reference MRI sequence was chosen as the first frame of the fully sampled data. The stepsize parameters of the proposed J-PDAL were fixed to $\sigma^0 = 1$, $\alpha = 0.5$, $\epsilon = 0.99$. The performance of different algorithms was evaluated using the root mean square error (RMSE) and the image structure similarity index (SSIM) [35]. The two metrics are expressed as below

$$\text{RMSE} = \sqrt{E(\|\hat{\mathbf{f}} - \mathbf{f}\|_2^2)} \quad (42)$$

$$\text{SSIM} = \frac{(2\mu_{\hat{\mathbf{f}}}\mu_{\mathbf{f}} + c_1)(2\sigma_{\hat{\mathbf{f}}\mathbf{f}} + c_2)}{(\mu_{\hat{\mathbf{f}}}^2 + \mu_{\mathbf{f}}^2 + c_1)(\sigma_{\hat{\mathbf{f}}}^2 + \sigma_{\mathbf{f}}^2 + c_2)} \quad (43)$$

where \mathbf{f} , $\hat{\mathbf{f}}$ are the ground truth and the estimated MRI sequences respectively, $E(\cdot)$ is the arithmetic mean, μ_a and σ_a^2 are the average and variance of variable a ($a \in \{\hat{\mathbf{f}}, \mathbf{f}\}$), $\sigma_{\hat{\mathbf{f}}\mathbf{f}}$ is the covariance between $\hat{\mathbf{f}}$ and \mathbf{f} , c_1 and c_2 are two constants to stabilize the division with small denominator.

Experiments in this section were performed using MATLAB 2016A on a 64 bit Linux platform with Intel(R) Core(TM) i7-6700K CPU @4.00GHz and 48 GB RAM.

A. Simulated PINCAT

The simulated PINCAT is of size $110 \times 100 \times 50$ with 50 temporal frames. A Golden angle radial sampling pattern with 20 rays per frame is used in this experiment. The regularization parameters of the proposed J-PDAL are $\tau = \eta = 5 \times 10^{-4}$, $\gamma = \lambda = 1 \times 10^{-5}$. The varying brightness weight $\mu = 3$ and the scale number for the motion estimation is $j = 5$.

Fig. 1 shows one example frame in spatial domain ($x-y$) and temporal frame ($x-t$) of the simulated fully-sampled data, the reference frame f_0 and the reconstructed DMRI using FISTA, kt-SLR, L+S, DC-CS and the proposed J-PDAL. Note that the image prior for f used in FISTA and J-PDAL is “l+TV” since the reconstruction performance using this regularization “l+TV” outperforms the reconstruction quality using other priors. Fig. 2 depicts the reconstruction performance comparison on the simulated PINCAT dataset using different algorithms. Specifically, J-PDAL is superior to FISTA using the same priors. The DMRI reconstruction quality using the joint prior “l+TV” outperforms that with other priors in both FISTA and J-PDAL frameworks. Furthermore, J-PDAL using the joint prior “l+TV” outperforms kt-SLR, L+S and DC-CS in terms of reconstruction quality, evaluated by RMSE and SSIM. Fig. 3 displays the motion vectors d and varying brightness q estimated using the proposed algorithm. Note that the boundary effects (no motion at boundaries) in the motion estimation is because the motion vectors and brightness variable are estimated at a coarse scale, where the image is downsampled by a factor of 2^j . The larger the scale number j , the more severe the boundary effects are.

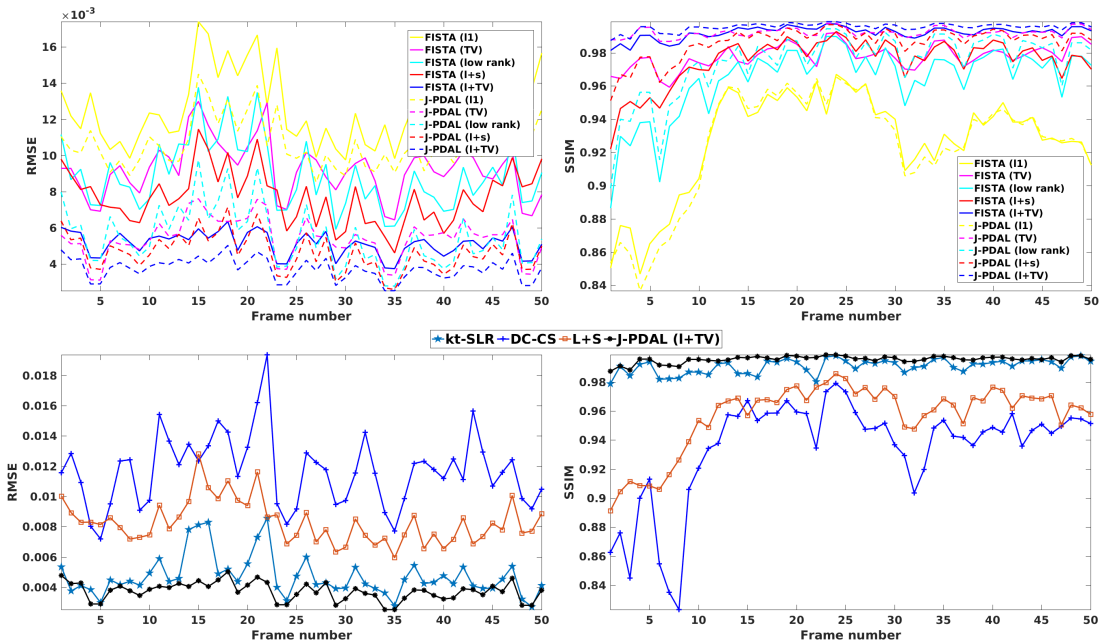


Fig. 2. Comparisons on simulated PINCAT. Top: The solid lines and dash lines represent the performance of MRI reconstruction using FISTA and the proposed J-PDAL with different priors in terms of the RMSE (left) and SSIM (right). Bottom: RMSEs (left) and SSIMs (right) of the reconstructed DMRI using kt-SLR, DC-CS, L+S and J-PDAL (with prior “l+TV”) at each time frame.

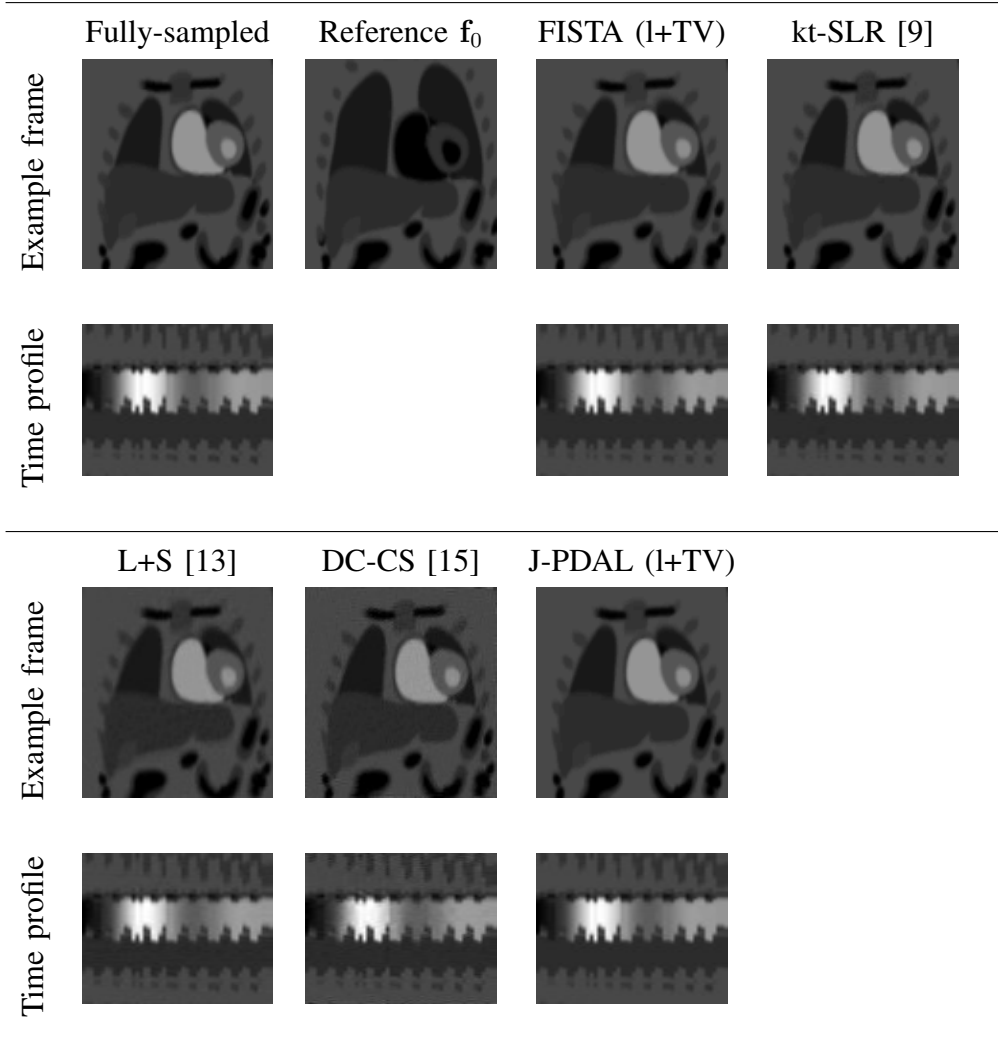


Fig. 1. From left (up) to right (down): fully-sampled PINCAT, reference image \bar{f}_0 , reconstructed DMRI using FISTA, kt-SLR, L+S, DC-CS and the proposed J-PDAL. In FISTA and J-PDAL, the priors for the DMRI \mathbf{f} considered are the combination of low rank and TV (“l+TV”).

B. Coronal lung MRI

The *in vivo* coronal lung data was recorded with a 1.5T Siemens Sonata Vision using spin echo (SE) sequences. The coronal lung data is of size $192 \times 192 \times 40$ with pixel-size 2.08×2.08 mm per frame and 40 temporal frames. The slice thickness is 7 mm. In this experiment, the fully-sampled data was subsampled using a golden angle radial sampling pattern [36] with 24 rays per frame. The regularization parameters of the proposed J-PDAL are $\tau = \eta = 5 \times 10^{-4}$, $\gamma = \lambda = 1 \times 10^{-5}$. The varying brightness weight is $\mu = 3$ and the scale number for the motion estimation is $j = 4$.

In Fig. 4, one example frame in spatial domain (x - y) and temporal frame (x - t) of the fully-

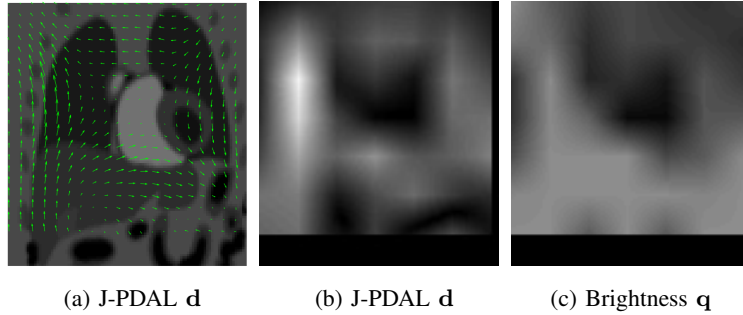


Fig. 3. Motion estimation for one example frame of the PINCAT using J-PDAL. (a) Estimated motion vectors shown in quiver form; (b) Magnitude of the estimated displacement field; (c) Varying brightness q .

sampled coronal lung data, the reference MRI and the initialization of all the algorithms are displayed. Fig. 4 also shows the reconstructed coronal lung data using kt-SLR [9], L+S [13], DC-CS [15], FISTA and the proposed J-PDAL. Note that the reconstructed DMRI using FISTA and J-PDAL shown in Fig. 4 were obtained with the DMRI prior “l+s” since the restoration performance using “l+s” prior in both FISTA and J-PDAL outperforms the performance using other priors.

Fig. 5 depicts the reconstruction performance comparison using different algorithms. The first row depicts the RMSEs and SSIMs using J-PDAL (dashed line) and the traditional CS-based scheme (solid lines, implemented using FISTA) with different priors at each time frames. The second row shows the reconstruction performance using kt-SLR [9], L+S [13], DC-CS [15] and the proposed J-PDAL with prior “l+s”. According to Fig. 5, the proposed J-PDAL outperforms the traditional CS scheme when the same priors are considered. Moreover, the proposed J-PDAL outperforms several state-of-the-art algorithms in terms of the RMSE and SSIM at each time frame. Fig. 6 displays the estimated motion vectors and the varying brightness map using J-PDAL.

C. Sagittal lung MRI

The *in vivo* sagittal lung data was also recorded on a 1.5T Siemens Sonata Vision with spin echo (SE) sequences. The sagittal lung MRI data is of size $128 \times 88 \times 80$ with pixel-size 3.125×3.125 mm per frame and 80 temporal frames. The slice thickness is 7 mm. A golden angle radial sampling pattern with 15 rays per frame is used in this experiment. The regularization parameters of the proposed J-PDAL are $\tau = \eta = 5 \times 10^{-4}$, $\gamma = \lambda = 1 \times 10^{-5}$. The varying brightness weight $\mu = 3$ and the scale number for the motion estimation is

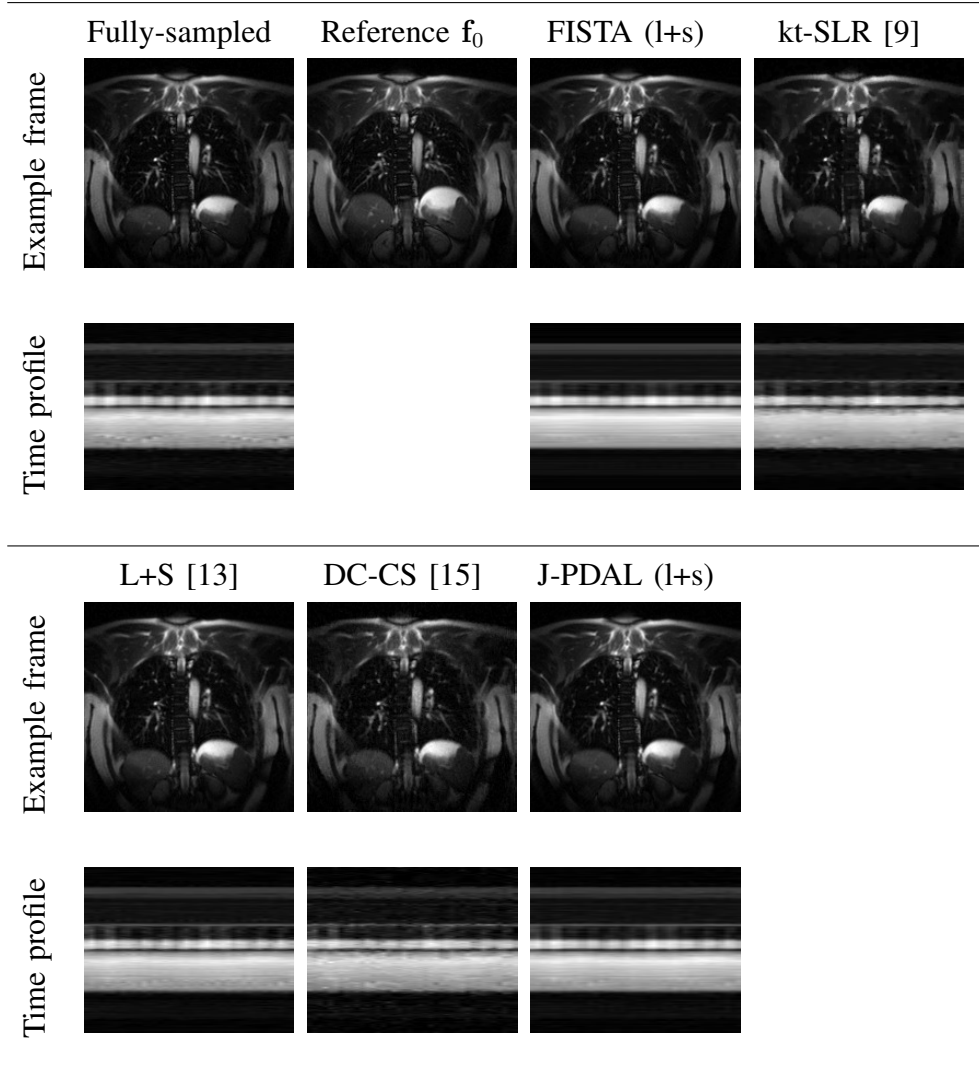


Fig. 4. From left to right: fully-sampled coronal lung data, reference image \bar{f}_0 , reconstructed DMRI using FISTA, kt-SLR, L+S, DC-CS and the proposed J-PDAL. In FISTA and J-PDAL, the priors for the DMRI \mathbf{f} considered are the combination of low rank and sparsity (“l+s”).

$j = 3$. Fig. 7 shows the fully-sampled sagittal lung data, the reference MRI and the restored MRI using FISTA, kt-SLR [9], L+S [13], DC-CS [15] and the proposed J-PDAL. Note that the reconstructed DMRI using FISTA and J-PDAL shown in Fig. 7 were obtained with the DMRI prior “l+s” since the restoration performance using “l+s” prior in both FISTA and J-PDAL outperforms the performance using other priors.

The quantitative comparisons between different DMRI reconstruction algorithms and the proposed J-PDAL on the sagittal lung data are depicted in Fig. 8. Similar to the coronal lung data, the restoration performance of the J-PDAL outperforms the existing CS-scheme using

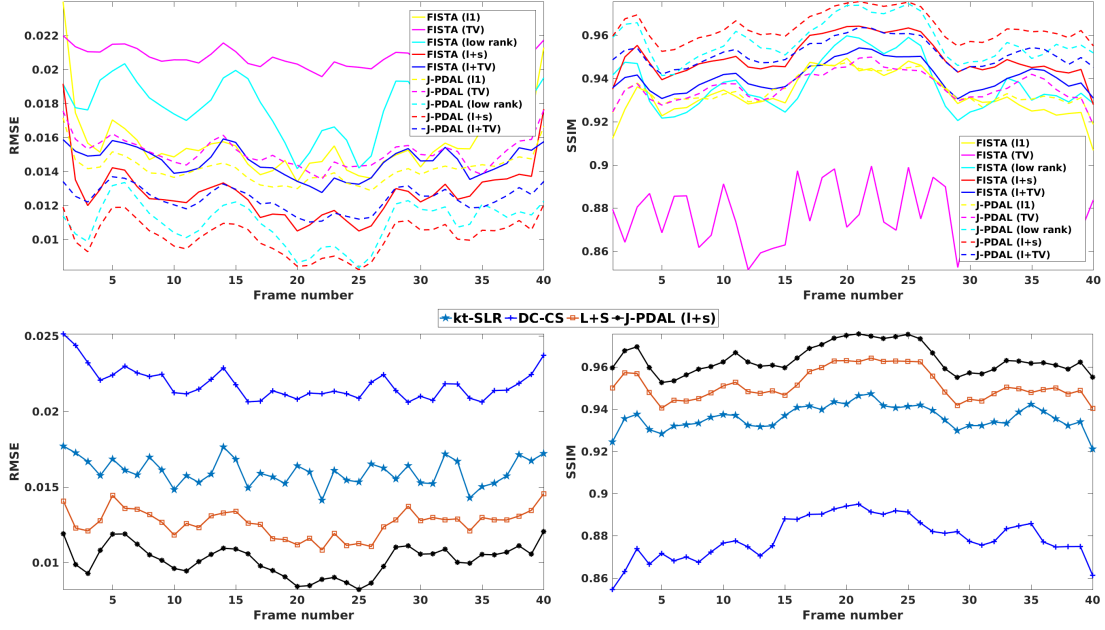


Fig. 5. Comparisons on *in vivo* coronal lung MRI reconstruction using different algorithms. Top: The solid line and dash line represent the performance of MRI reconstruction using FISTA and the proposed J-PDAL in terms of the RMSE (left) and SSIM (right). Bottom: Comparisons on *in vivo* coronal lung MRI using different state-of-the-art algorithms (kt-SLR, DC-CS, L+S) and the proposed J-PDAL in terms of the RMSE (left) and SSIM (right) for each temporal frame. The prior considered in the proposed J-PDAL method is “l+s”.

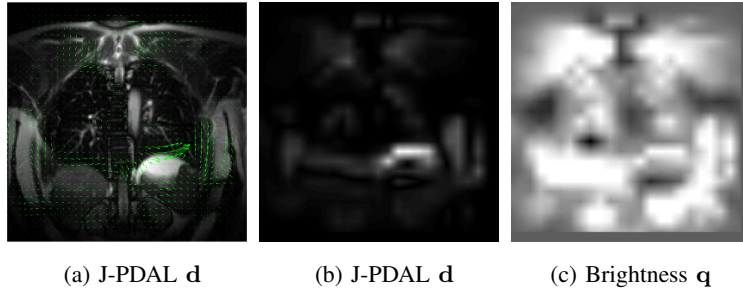


Fig. 6. Motion estimation for one example frame of the coronal lung MRI. (a) Estimated motion vectors shown in quiver form; (b) Magnitude of the estimated motion displacement field; (c) varying brightness \mathbf{q} . The arrows in (a) have been stretched with a scale parameter $\times 3$ for better visualization.

the same priors in terms of RMSE and SSIM. Moreover, the reconstruction quality using the prior “l+s” is superior to the quality obtained using other priors. According to the second row of Fig. 8, the reconstruction performance of the proposed J-PDAL with prior “l+s” is superior to kt-SLR and DC-CS, while the reconstruction result using L+S is competitive to

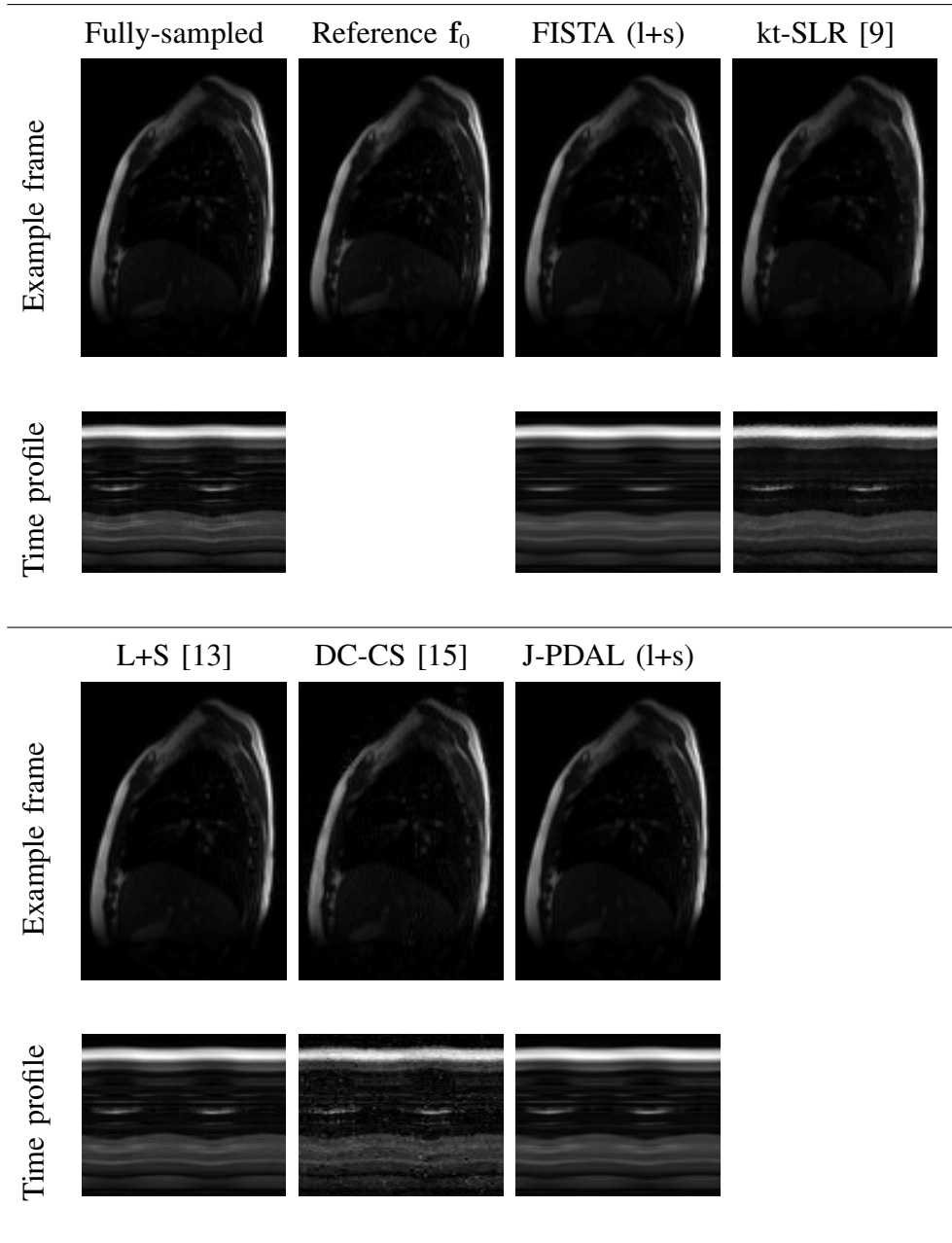


Fig. 7. From left to right: fully-sampled sagittal lung data, reference image \bar{f}_0 , reconstructed DMRI using FISTA, kt-SLR, L+S, DC-CS and the proposed J-PDAL. In FISTA and J-PDAL, the priors for the DMRI \mathbf{f} considered are the combination of low rank and sparsity (“l+s”).

that of J-PDAL in terms of RMSE and SSIM at each time frame.

The motion vectors \mathbf{d} and the varying brightness variable \mathbf{q} for the *in vivo* sagittal lung data are displayed in Fig. 9. Similar to previous experiments, there are boundary effects (no motion at boundaries) in Fig. 9, which is due to the downsampling process during the motion estimation.

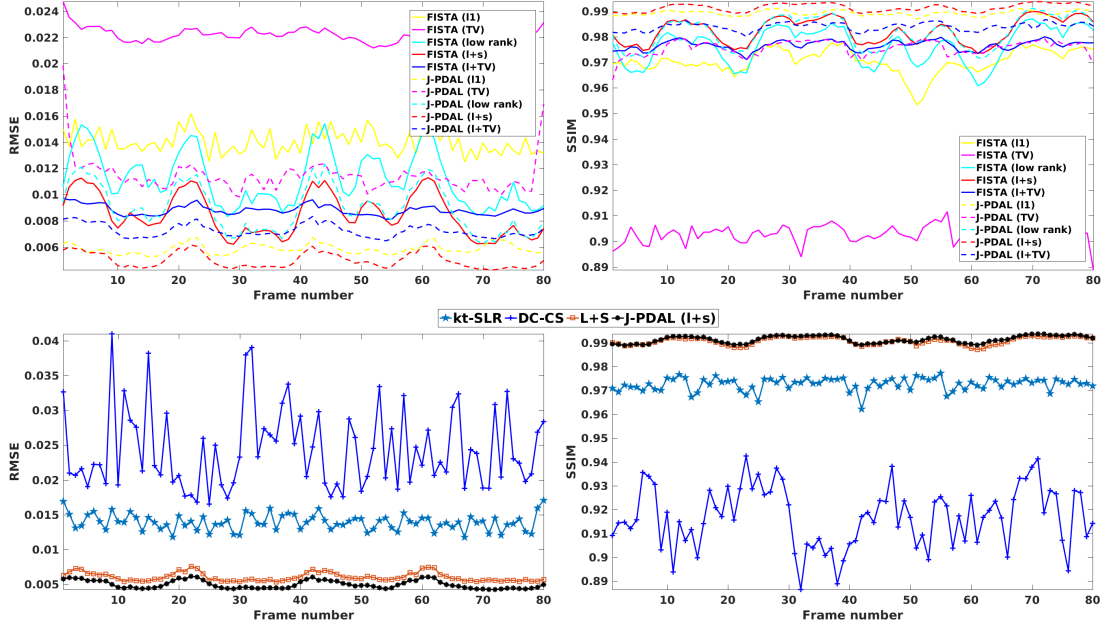


Fig. 8. Comparisons on *in vivo* sagittal lung MRI. Top: The solid lines and dash lines represent the performance of MRI reconstruction using FISTA and the proposed J-PDAL in terms of the RMSE (left) and SSIM (right). Bottom: RMSEs (left) and SSIMs (right) of the reconstructed DMRI using kt-SLR, DC-CS, L+S and J-PDAL (with prior “l+s”) at each time frame.

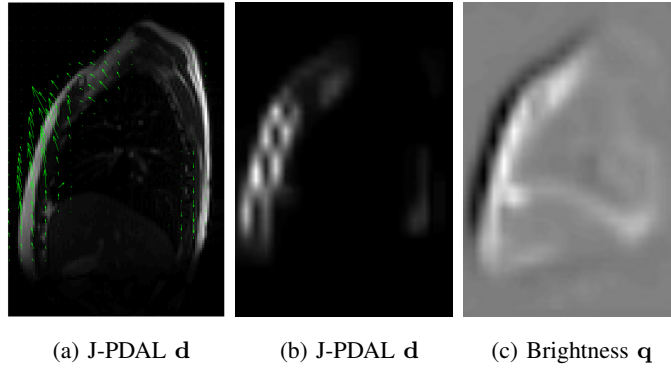


Fig. 9. Motion estimation of the coronal lung MRI. (a) Estimated motion vectors shown in quiver form; (b) Magnitude of the estimated motion displacement field; (c) varying brightness \mathbf{q} . The arrows in (a) have been stretched with a scale parameter $\times 2$ for better visualization.

VI. CONCLUSIONS

This paper proposed a novel framework to jointly reconstruct the DMRI and estimate the motion vectors by embedding the intensity based optical flow constraint into the compressed sensing framework. The proposed framework is able to deal with a wide class of image

priors for DMRI reconstruction. Moreover, a parametric/affine model was introduced to model realistic motion patterns in DMRI. The estimation of the corresponding motion parameters has been conducted at a coarse scale instead of the finest scale. The choice of the scale number is related with the data. Note that a large coarse scale can overlook small objects, while a small scale can lead to ambiguous motion estimation. The formulated problem is then addressed using a primal dual algorithm with linesearch (denoted as “J-PDAL”). We demonstrated that the proposed algorithm is superior to the traditional compressed sensing scheme for DMRI reconstruction (implemented with FISTA) using the same image priors. Moreover, the proposed algorithm with appropriate priors outperforms several state-of-the-art algorithms. Among the datasets explored in this paper, the most appropriate priors for the *in vivo* lung data are the combination of low rank and sparsity in temporal frequency domain (“l+s”), while the most appropriate priors for the *in vivo* perfusion cardiac MRI are the combination of the low rank and total variation (“l+TV”). It is also interesting to note that the motion estimation at a coarse scale can lead to boundary effects (no motion at the boundaries) due to the downsampling procedure when dealing with the optical flow constraint at a coarse scale.

Future work includes the exploration of phase based optical flow instead of the intensity based optical flow. Multi-scale methods will also be combined to improve the accuracy of motion estimation.

ACKNOWLEDGEMENTS

This work has been supported by NIH grant R01CA188300.

REFERENCES

- [1] P. Mansfield, “Multi-planar image formation using NMR spin echoes,” *Journal of Physics C: Solid State Physics*, vol. 10, no. 3, p. L55, 1977. [Online]. Available: <http://stacks.iop.org/0022-3719/10/i=3/a=004>
- [2] A. Haase, J. Frahm, D. Matthaei, W. Hnicke, and K.-D. Merboldt, “FLASH imaging: Rapid NMR imaging using low flip-angle pulses,” *J. Magn. Reson.*, vol. 213, no. 2, pp. 533 – 541, 2011, magnetic Moments. [Online]. Available: <http://www.sciencedirect.com/science/article/pii/S1090780711003338>
- [3] J. Tsao and S. Kozerke, “MRI temporal acceleration techniques,” vol. 36, no. 3, pp. 543–560, 2012.
- [4] M. Lustig, D. Donoho, and J. M. Pauly, “Sparse MRI: The application of compressed sensing for rapid MR imaging,” vol. 58, no. 6, pp. 1182–1195, 2007.
- [5] J. M. Lustig, Michael and Donoho, David L and Santos, Juan M and Pauly, “Compressed sensing MRI,” *IEEE Sig. Process. Mag.*, vol. 25, no. 2, pp. 72–82, 2008.
- [6] H. Jung, K. Sung, K. S. Nayak, E. Y. Kim, and J. C. Ye, “K-t FOCUSS: A general compressed sensing framework for high resolution dynamic MRI,” vol. 61, no. 1, pp. 103–116, 2009.

- [7] F. Knoll, C. Clason, K. Bredies, M. Uecker, and R. Stollberger, "Parallel imaging with nonlinear reconstruction using variational penalties," vol. 67, no. 1, pp. 34–41, 2012.
- [8] X. Miao, S. G. Lingala, Y. Guo, T. Jao, M. Usman, C. Prieto, and K. S. Nayak, "Accelerated cardiac cine MRI using locally low rank and finite difference constraints," *Magn. Reson. Imaging*, vol. 34, no. 6, pp. 707–714, 2016. [Online]. Available: <http://dx.doi.org/10.1016/j.mri.2016.03.007>
- [9] S. G. Lingala, Y. Hu, E. Dibella, and M. Jacob, "Accelerated dynamic MRI exploiting sparsity and low-rank structure: K-t SLR," *IEEE Trans. Med. Imag.*, vol. 30, no. 5, pp. 1042–1054, 2011.
- [10] A. Majumdar, "Real-time Dynamic MRI Reconstruction using Stacked Denoising Autoencoder," 2015. [Online]. Available: <http://arxiv.org/abs/1503.06383>
- [11] B. Tremoulheac, N. Dikaios, D. Atkinson, and S. R. Arridge, "Dynamic MR image reconstruction-separation from undersampled (k,t)-Space via low-rank plus sparse prior," *IEEE Trans. Med. Imag.*, vol. 33, no. 8, pp. 1689–1701, 2014.
- [12] A. Majumdar, R. K. Ward, and T. Aboulnasr, "Compressed sensing based real-time dynamic MRI reconstruction," *IEEE Trans. Med. Imag.*, vol. 31, no. 12, pp. 2253–2266, 2012.
- [13] R. Otazo, E. Candès, and D. K. Sodickson, "Low-rank plus sparse matrix decomposition for accelerated dynamic MRI with separation of background and dynamic components," vol. 73, no. 3, pp. 1125–1136, 2015.
- [14] H. Jung and J. C. Ye, "Motion estimated and compensated compressed sensing dynamic magnetic resonance imaging: What we can learn from video compression techniques," *Int. J. Imaging Syst. Technol.*, vol. 20, no. 2, pp. 81–98, 2010.
- [15] S. G. Lingala, S. Member, E. Dibella, M. Jacob, and S. Member, "(DC-CS): A Novel Framework for Accelerated Dynamic MRI," *IEEE Trans. Med. Imag.*, vol. 34, no. 1, pp. 72–85, 2015.
- [16] L. Feng, L. Axel, H. Chandarana, K. T. Block, D. K. Sodickson, and R. Otazo, "XD-GRASP: Golden-angle radial MRI with reconstruction of extra motion-state dimensions using compressed sensing," vol. 75, no. 2, pp. 775–788, 2016.
- [17] H. Li, M. Haltmeier, S. Zhang, J. Frahm, and A. Munk, "Aggregated motion estimation for real-time MRI reconstruction," vol. 72, no. 4, pp. 1039–1048, 2014.
- [18] M. Sühling, M. Arigovindan, C. Jansen, P. Hunziker, and M. Unser, "Myocardial motion analysis from B-mode echocardiograms," *IEEE Trans. Image Process.*, vol. 14, no. 4, pp. 525–536, 2005.
- [19] Y. Malitsky and T. Pock, "A first-order primal-dual algorithm with linesearch," pp. 1–24, 2016. [Online]. Available: <http://arxiv.org/abs/1608.08883>
- [20] M. A. Bernstein, K. F. King, and X. J. Zhou, *Handbook of MRI Pulse Sequences*. Elsevier Academic Press, 2004.
- [21] J. L. Barron, D. J. Fleet, and S. S. Beuchemin, "Performance of optical flow techniques," *Int. J. Comput. Vis.*, vol. 12, no. 1, pp. 43–77, 1994.
- [22] A. Wedel, T. Pock, C. Zach, H. Bischof, and D. Cremers, *An Improved Algorithm for TV-L 1 Optical Flow*. Berlin, Heidelberg: Springer Berlin Heidelberg, 2009, pp. 23–45. [Online]. Available: https://doi.org/10.1007/978-3-642-03061-1_2
- [23] A. Chambolle and T. Pock, "A first-order primal-dual algorithm for convex problems with applications to imaging," *J. Math. Imag. Vision*, vol. 40, no. 1, pp. 120–145, 2011.
- [24] Y. Altunbasak, R. M. Mersereau, and A. J. Patti, "A fast parametric motion estimation algorithm with illumination and lens distortion correction," *IEEE Trans. Image Process.*, vol. 12, no. 4, pp. 395–408, 2003.
- [25] M. Alessandrini, A. Basarab, H. Liebgott, and O. Bernard, "Myocardial Motion Estimation from Medical Images Using the Monogenic Signal," *IEEE Trans. Image Process.*, vol. 22, no. 3, pp. 1084–1095, 2013.

- [26] D. Sun, S. Roth, and M. J. Black, "Secrets of optical flow estimation and their principles," in *Proc. IEEE Conference on Computer Vision and Pattern Recognition (CVPR)*, San Francisco, CA, USA, 2010.
- [27] N. Parikh and S. Boyd, "Proximal algorithms," *Foundations and Trends in Optimization*, vol. 1, no. 3, pp. 127–239, 2014. [Online]. Available: <http://dx.doi.org/10.1561/2400000003>
- [28] T. Pock, D. Cremers, H. Bischof, and A. Chambolle, "An algorithm for minimizing the mumford-shah functional," in *Computer Vision, 2009 IEEE 12th International Conference on*. IEEE, 2009, pp. 1133–1140.
- [29] N. Komodakis and J. C. Pesquet, "Playing with duality: An overview of recent primal-dual approaches for solving large-scale optimization problems," *IEEE Sig. Process. Mag.*, vol. 32, no. 6, pp. 31–54, 2015.
- [30] E. Esser, X. Zhang, and T. Chan, "A general framework for a class of first order primal-dual algorithms for tv minimization," *Ucla Cam Report*, pp. 09–67, 2009.
- [31] M. Sühling, M. Arigovindan, P. Hunziker, and M. Unser, "Multiresolution moment filters: Theory and applications," *IEEE Trans. Image Process. Wed*, vol. 13, no. 4, pp. 484–495, 2004.
- [32] M. Zhu and T. Chan, "An efficient primal-dual hybrid gradient algorithm for total variation image restoration," University of California, Los Angeles (UCLA), Tech. Rep., 2008.
- [33] B. Zhao, J. P. Haldar, A. G. Christodoulou, and Z.-P. Liang, "Image reconstruction from highly undersampled (k,t)-space data with joint partial separability and sparsity constraints," *IEEE Trans. Med. Imag.*, vol. 31, no. 9, pp. 1809–1820, 2012.
- [34] B. Sharif and Y. Bresler, "Physiologically improved NCAT phantom (PINCAT) enables in -silico study of the effects of beat-to-beat variability on cardiac MR," in *Proc. Annual Meeting of ISMRM*, Berlin, 2007.
- [35] Z. Wang, A. C. Bovik, H. R. Sheikh, and E. P. Simoncelli, "Image quality assessment: From error visibility to structural similarity," *IEEE Trans. Image Process.*, vol. 13, no. 4, pp. 600–612, 2004.
- [36] L. Feng, R. Grimm, K. T. Block, H. Chandarana, S. Kim, J. Xu, L. Axel, D. K. Sodickson, and R. Otazo, "Golden-angle radial sparse parallel MRI : Combination of compressed sensing , parallel imaging , and golden-angle radial sampling for fast and flexible dynamic volumetric MRI," vol. 72, pp. 707–717, 2014.